Molecular Dynamics Simulations of Arachidonic Acid-Derived Pentadienyl Radical Intermediate Complexes with COX-1 and COX-2: Insights into Oxygenation Regio- and Stereoselectivity†

Kristina E. Furse,[‡,§] Derek A. Pratt,[‡,||] Claus Schneider,[⊥] Alan R. Brash,[⊥] Ned A. Porter,[‡] and Terry P. Lybrand*[,‡,§,⊥]

Department of Chemistry, Center for Structural Biology, and Department of Pharmacology, Vanderbilt University, Nashville, Tennessee 37232

Received November 15, 2005; Revised Manuscript Received January 19, 2006

ABSTRACT: The two cyclooxygenase enzymes, COX-1 and COX-2, are responsible for the committed step in prostaglandin biosynthesis and are the targets of the nonsteroidal antiinflammatory drugs aspirin and ibuprofen and the COX-2 selective inhibitors, Celebrex, Vioxx, and Bextra. The enzymes are remarkable in that they catalyze two dioxygenations and two cyclizations of the native substrate, arachidonic acid, with near absolute regio- and stereoselectivity. Several theories have been advanced to explain the nature of enzymatic control over this series of reactions, including suggestions of steric shielding and oxygen channeling. As proposed here, selective radical trapping and spin localization in the substrate-derived pentadienyl radical intermediate can also be envisioned. Herein we describe the results of explicit, 10 ns molecular dynamics simulations of both COX-1 and COX-2 with the substrate-derived pentadienyl radical intermediate bound in the active site. The enzymes' influence on the conformation of the pentadienyl radical was investigated, along with the accessible space above and below the radical plane and the width of several channels to the active site that could function as access routes for molecular oxygen. Additional simulations demonstrated the extent of molecular oxygen mobility within the active site. The results suggest that spin localization is unlikely to play a role in enzymatic control of this reaction. Instead, a combination of oxygen channeling, steric shielding, and selective radical trapping appears to be responsible. This work adds a dynamic perspective to the strong foundation of static structural data available for these enzymes.

Polyunsaturated fatty acid oxidation has long been of interest to chemists and biochemists due to its importance in industry and human health. Both enzymatic pathways and abiotic chain reactions have been identified and studied extensively, and a consensus has developed on many aspects of the mechanisms involved (*1*−*3*). The enzymes that oxygenate these lipids in mammals and other higher animals belong to the cyclooxygenase (COX)[1] and lipoxygenase (LOX) families. The natural substrate in both cases is arachidonic acid (AA or 5*Z*,8*Z*,11*Z*,14*Z*-eicosatetraenoic acid), which is converted to prostaglandin H_2 (PGH_2) by both isoforms of COX and to various hydroperoxyeicosatetraenoic acids (HPETEs) by the different LOX isoforms. The conversion of AA to PGH_2 by COX is a particularly relevant process, as it represents the committed step in prostaglandin biosynthesis. Subsequent transformations of PGH_2 by downstream prostaglandin synthases produce a family of prostaglandins, thromboxane and prostacyclin, which play major roles in cellular homeostasis as well as in mediation of the inflammatory response (*4*). While the COX-1 isoform is generally considered to be constitutively expressed and responsible for the former "housekeeping" functions, COX-2 expression is induced in response to a variety of stimuli, and its inhibition appears to produce the analgesic, antipyretic, and antiinflammatory effects of the nonsteroidal antiinflammatory drugs (NSAIDs).

The nonenzymatic (solution) oxidation of AA or its esters yields many products. Mechanistic studies of the radical-mediated autoxidation of AA and linoleic acid (LA or 9*Z*,12*Z*-octadecadienoic acid) have accounted for the formation of most of these products. We summarize the findings for LA oxidations in Scheme 1 (*3*, *5*−*7*). Abstraction of hydrogen from the bisallylic methylene carbon forms a planar intermediate pentadienyl radical with positive unpaired electron spin density at carbons 1, 3, and 5 of the five-carbon unit (*8*). Oxygen can add to the planar radical from either face, resulting in two possible enantiomers for each hydroperoxide product. In the absence of good peroxyl radical-trapping agents such as a phenol, the *E*,*E*-hydroperoxides, **3**

† This work was supported in part by NIH Grants NS33290 (T.P.L.), HL17921 (N.A.P.), and GM53638 (A.R.B.). K.E.F. was supported by Training Grant T32 GM08320 from the National Institutes of Health and by the Warren Fellowship. D.A.P. was supported by NSERC Canada and the Warren Fellowship.

* To whom correspondence should be addressed. Tel: (615) 343-1247. Fax: (615) 936-2211. E-mail: terry.p.lybrand@vanderbilt.edu.

‡ Department of Chemistry.

§ Center for Structural Biology.

|| Current address: Department of Chemistry, Queen's University, Kingston, Ontario, Canada K7L 3N6.

⊥ Department of Pharmacology.

[1] Abbreviations: COX, cyclooxygenase; MD, molecular dynamics; NSAIDs, nonsteroidal antiinflammatory drugs; AA, arachidonic acid; AA-13-yl, arachidonic acid-derived pentadienyl radical intermediate; PGG_2, prostaglandin G_2; PGH_2, prostaglandin H_2; HETE, hydroxyeicosatetraenoic acid; HPETE, hydroperoxyeicosatetraenoic acid; RMSD, root mean square deviation.

10.1021/bi052338h CCC: $33.50
Published on Web 02/17/2006

Scheme 1: Solution Autoxidation of Linoleic Acid or Its Esters

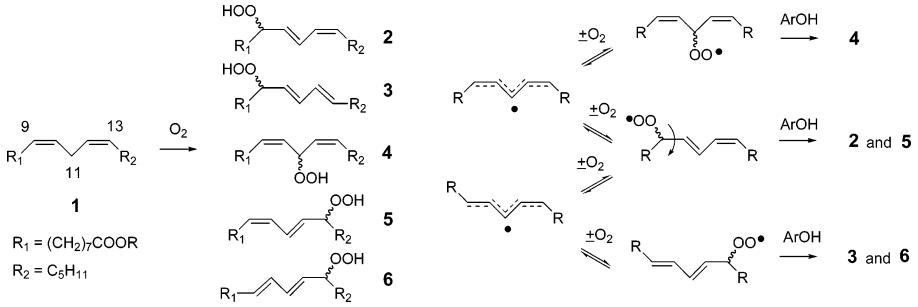

Scheme 2: Secondary Oxidation Products of AA

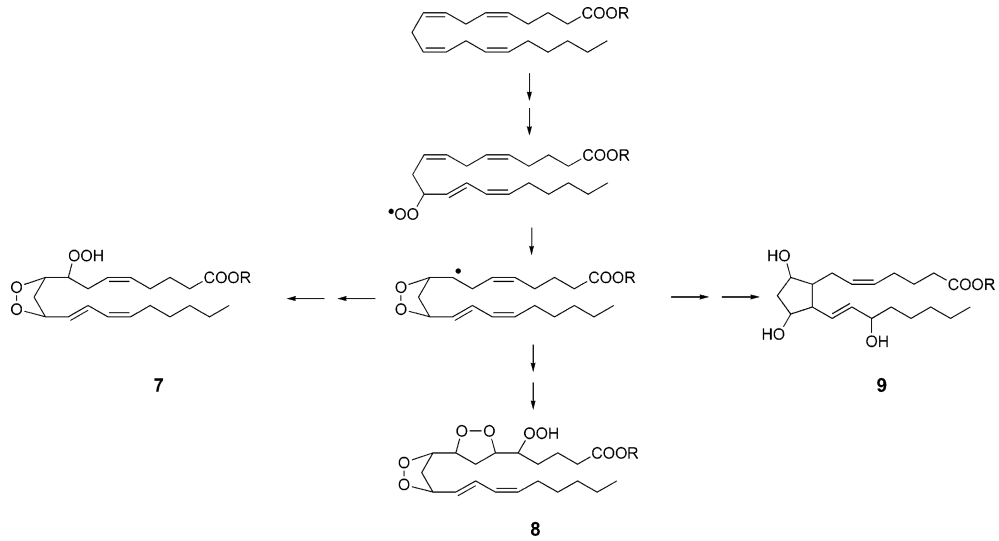

and **6**, can be formed to a greater extent than the *Z,E*-hydroperoxides, **2** and **5** (*9*). Under conditions where a good hydrogen atom donor is present, the mechanism leading to **3** and **6** is shut down, and now, in addition to **2** and **5**, some nonconjugated hydroperoxides (**4**) appear (*7*). AA has three bisallylic methylene carbons and, thus, three possible *Z,Z*-pentadienyl radicals to which oxygen can add to yield hydroperoxides. The picture is further complicated when one considers that the 8-, 9-, 11-, and 12-peroxyl radicals of arachidonate can cyclize to yield endoperoxides in competition with reduction to the hydroperoxides, leading to monocyclic peroxides (e.g., **7**), serial cyclic peroxides (e.g., **8**), and isoprostanes [e.g., **9** (Scheme 2)] (*5*, *10*, *11*).

In stark contrast to the diverse regio- and stereochemical outcomes of the solution phase autoxidation of AA, the COX-mediated oxidation yields only the bicyclic endoperoxide PGG_2 and small amounts of minor monohydroxy acid products, 11*R*-hydroperoxy-5*Z*,8*Z*,12*E*,14*Z*-eicosatetraenoic acid (11*R*-HPETE) and 15*R*/*S*-hydroperoxy-5*Z*,8*Z*,11*Z*,13*E*-eicosatetraenoic acid (15*R*-HPETE and 15*S*-HPETE) (*12*, *13*). The mechanism of the "cyclooxygenase reaction", which leads to the intermediate PGG_2, is shown in Scheme 3 along with the subsequent "peroxidase reaction", reduction of the C15 hydroperoxide of PGG_2 to the corresponding alcohol, PGH_2, which occurs at a different, but redox-coupled active site (*1*, *14*). Here, we have focused our attention on the exquisite regio- and stereochemical control exerted by the enzyme over the cascade of radical reactions that leads to PGG_2, beginning with oxygenation of the putative C11−C15 pentadienyl radical, whose generation following abstraction of the C13 *pro-S* H-atom by the catalytic tyrosyl-385 radical (Tyr-385•) is the rate-limiting step in PGH_2 biosynthesis (*15*).

Over the past 40 years, experimental work, including X-ray crystallography, site-directed mutagenesis, and electron paramagnetic resonance (EPR) spectroscopic studies, has provided substantial insight into the structural basis of COX catalysis (*1*, *16*). In 1967, Hamberg and Samuelsson established that COX selectively abstracts the *pro-S* hydrogen from the C13 methylene carbon of AA, creating a C11−C15 pentadienyl radical selectively over potential C5−C9 or C8−C12 radicals, thereby eliminating approximately two-thirds of the possible products derived from primary autoxidation of AA (*15*). The positioning of C13 closest to Tyr-385 in the 2000 X-ray crystal structure of AA bound to COX-1 demonstrated structurally how the enzyme selectively oxygenates the C11−C15 pentadiene unit (*17*). However, the question still remains: given that the C11−C15 pentadienyl radical is formed and can be observed by EPR spectroscopy (*18*, *19*), why does oxygen add almost exclusively to the *pro-R* face of C11? We have identified four possible scenarios that deserve consideration in answering this question: (i) molecular oxygen is directed to the substrate via a designated oxygen channel in the enzyme leading to preferential oxygenation of the radical intermediate at the *pro-R* face of C11; (ii) the substrate is bound in the active site in a conformation that prevents access of molecular oxygen to all positive spin-bearing positions along the pentadienyl radical but the *pro-R* face of C11 (*20*, *17*); (iii) the enzyme can bias the spin distribution in the radical

Scheme 3: COX-Catalyzed Conversion of AA to PGH_2

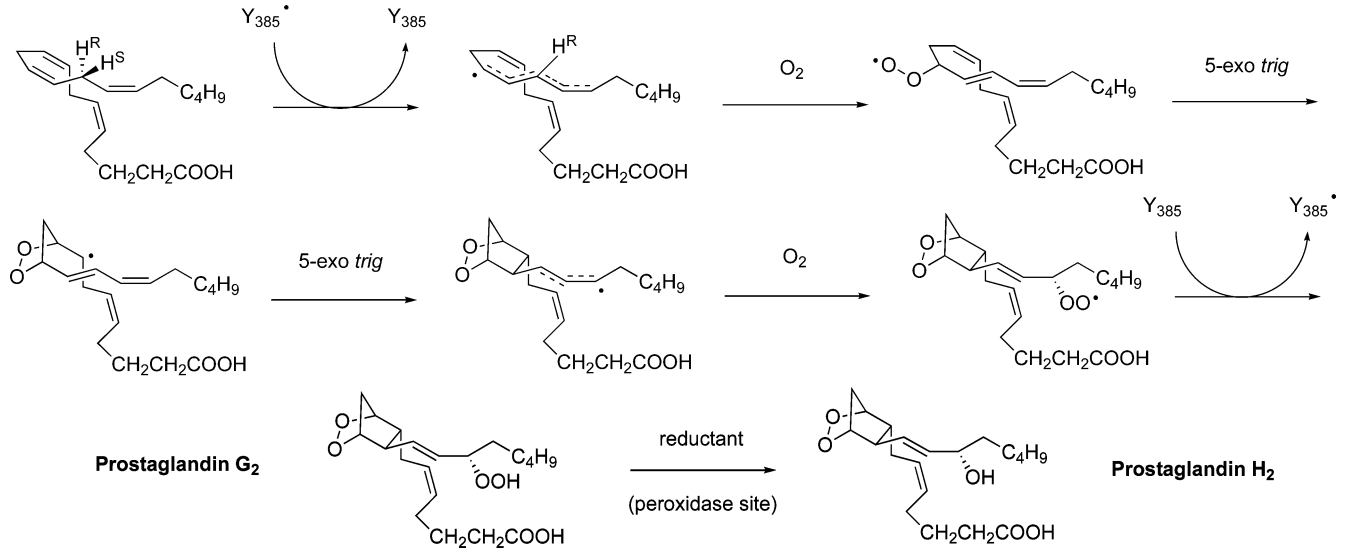

intermediate by forcing it to adopt a higher energy conformation which localizes the spin at the *pro-R* face of C11; (iv) simple competition kinetics governs the product distribution; oxygen adds to all possible positions along the substrate radical to generate six intermediate peroxyl radicals, with only oxygenation at the *pro-R* face of C11 yielding an intermediate that can be efficiently trapped (via cyclization to form the endoperoxide ring).

In this work, we use molecular dynamics (MD) to build on the strong foundation provided by X-ray crystallography, site-directed mutagenesis, and EPR spectroscopy to test the likelihood of these possible control mechanisms. Our prior simulation work with COX/AA complexes [see accompanying paper (*50*)] characterized the equilibrium behavior of the enzyme−substrate complexes and demonstrated good agreement with experimental results, laying the groundwork for the current investigation of theoretical complexes of the AA-derived pentadienyl radical intermediate (AA-13-yl) with the COX enzymes.

METHODS

Parameter Development. The open-shell, delocalized C11−C15 pentadienyl radical of the AA-13-yl intermediate is not well represented by parameters available in the standard AMBER ff99 force field (*21*), so new parameters were derived. Four new atom types, C7, C8, C9, and HX, were created for this intermediate, so that AA-13-yl atoms C11−C12−C13−C14−C15 are represented by types C7−C8−C9−C8−C7, with attached hydrogens of type HX. A gas-phase minimum energy structure for the AA-13-yl radical was generated by Hartree−Fock molecular orbital calculations with a 6-31G* basis set using Gaussian98 (*22*). Equilibrium bond lengths were taken directly from this minimum energy structure, and force constants were interpolated using reference values in the ff99 force field (*21*). Parameters describing the homoconjugated double bonds from C5−C9 were taken from our previous work with AA. New torsional parameters were needed to model the dihedral angles for AA-13-yl radical fragments CT-C7−C8−C9 and C7−C8−C9−C8 (where CT is the standard AMBER sp^3 atom type). Torsion energy profiles were calculated over the range 0−360° using density functional theory at the B3LYP/6-31G* level of theory (*23*). Potential function parameters were then adjusted to reproduce the quantum mechanical torsion profiles. A molecular electrostatic potential for the AA-13-yl radical was calculated over a grid of points using the Hartree−Fock optimized geometry and a 6-31G* basis set. Partial charges were derived by fitting the electrostatic potential to an atom-centered point charge model according to the procedure of Cornell et al. (*24*).

Homodimer Model Setup and Simulation. Static structures taken ∼500 ps into the equilibration phase of our previous MD simulations of the ovine COX-1/AA and murine COX-2/AA complexes were used to generate the initial models for the current investigation. These systems consisted of the homodimer, two heme groups, two AA molecules, and eight detergent molecules, solvated in truncated octahedron periodic boxes of explicit water molecules and sodium counterions, resulting in systems of 104234 and 118858 atoms for COX-1 and COX-2, respectively. The C13 *pro-S* hydrogen atom of each of the two AA molecules bound per COX homodimer was removed, and 9−10 ns isothermal−isobaric ensemble MD simulations were run using AMBER 7.0 (*25*) with the AMBER ff99 force field (*21*) and the SPC/E (*26*) water model. All covalent bonds containing hydrogen were fixed at equilibrium lengths using the SHAKE algorithm (*27*). A 1 fs integration time step was used for all simulations, and configurations were collected every 1 ps for subsequent analysis. Constant temperature and pressure were maintained via weak coupling to a thermal reservoir (tautp = 1.0 ps) and Berendsen piston (taup = 1.0 ps) (*28*). A 9 Å real-space nonbonded cutoff was used in all simulations, and a particle mesh Ewald summation method was used to compute long-range electrostatic energy and force corrections (*29*). All MD trajectories were analyzed visually using MDDISPLAY (*30*), and most numerical analyses were performed with the ptraj module of AMBER.

Extensive studies of the stability of the simulations of AA complexes of COX-1 and COX-2 were detailed in our previous study. Structural fluctuations for the complexes of AA-13-yl bound to COX-1 and COX-2 in the current study were also well behaved and consistent over the full simula-

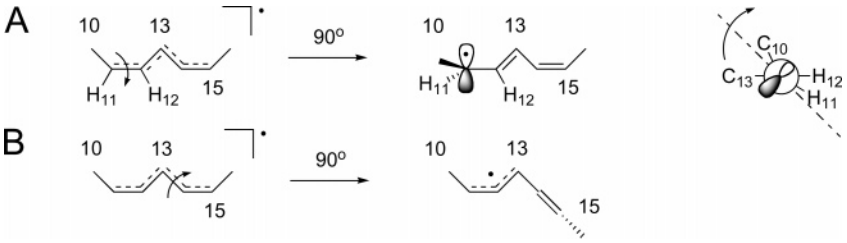

FIGURE 1: Torsion about the C11−C12 bond (A) of the AA-derived C11−C15 pentadienyl radical intermediate localizes spin to the *pro-R* face of C11, while torsion about the C12−C13 or C13−C14 bond (B) leads to an allyl radical.

tions and therefore will not be discussed explicitly here (see Supporting Information for plots of root mean square deviations relative to crystal structure models).

In addition to the unbiased MD simulations, biased MD simulations followed by potential of mean force (PMF) calculations were undertaken to further probe the impact of the enzyme on the torsional behavior of the AA-13-yl radical. This procedure can be used to compare the energy barrier along some reaction coordinate in different environments. A harmonic biasing potential of 100 kcal/(mol·radian^2) [0.0609 kcal/(mol·deg^2)] was used to overcome the intrinsic energy barrier and force the C10−C11−C12−C13 (heretofore referred to as C11−C12) torsion angle to sample the entire range from 0 to 90° while bound to the enzyme. The range was divided into 19 separate windows in which the harmonic potential was used to hold the C11−C12 torsion to a target value (0°, 5°, 10°, ..., 90°). For each window, an MD simulation was run in which the C11−C12 torsion was driven to the new target value (e.g., 0° → 5°) over the course of 10 ps and equilibrated for 40 ps, followed by 50 ps of data collection at 0.1 ps intervals. Torsion values were extracted using ptraj. The resulting data set, 19 windows of 500 torsion angles each, was analyzed using the weighted histogram analysis method (WHAM) (*31*, *32*) to remove the biasing potential and estimate the energy barrier, or PMF, for the enzyme-bound torsion. This procedure was repeated for the AA-13-yl radical in a periodic water box with a sodium counterion to establish a control PMF profile for the substrate free in solution. The same protocol was used to calculate the free and enzyme-bound PMF profiles for the C12−C13−C14−C15 (C13−C14) torsion angle from 90° to 270°.

Channel Analysis. A survey of potential oxygen access channels was performed over the course of the trajectory using the channel_finder utility as described in detail in the accompanying paper. The channel analysis involves iterative calculations of the solvent-accessible surface using probe spheres of varying radii. The surface calculation is initiated within the enzyme active site with all but one potential exit route blocked. The largest probe sphere radius that can exit the protein interior gives an estimate of the radius of the channel through which it escaped. Molecular surfaces were calculated with the MSMS program (*33*), and the analyses were performed over the final 7.4 ns of each trajectory.

In addition to the channel measurements, several short simulations were run with an explicit molecule of oxygen placed in each active site in order to observe O_2 mobility within the enzyme and detect exit events through the putative oxygen channels. Static structures taken 800 ps into the current simulations of COX-1/AA-13-yl and COX-2/AA-13-yl complexes were used to generate the initial models. A molecule of oxygen was placed near the *pro*-R face of C11, the predominant site of the first oxygen addition. The complexes were then energy minimized for 300 steps using a steepest decent gradient method to relieve any small steric clashes potentially introduced by the oxygen addition. These structures were used as the starting points for five 500 ps simulations for each COX isoform. Each simulation was assigned a different initial Boltzmann velocity distribution in order to create unique trajectories. For each completed simulation, the protein backbone was RMS fitted to the starting structure to remove any rotational motion, and the Cartesian coordinates of oxygen across the trajectory were collected in a single PDB (Protein Data Bank format) file. The geometric primitives feature of DINO (*34*) was then used to draw lines connecting sequential O_2 positions in order to trace the path of oxygen over time.

Steric Shielding Analysis. A new protocol was developed in order to quantify the degree of steric shielding above and below the AA-13-yl radical plane across the COX-1 and COX-2 trajectories. For each snapshot, five slightly overlapping virtual boxes were created along both faces of the pentadienyl radical intermediate (C11−C15), and the closest enzyme atom in each box was identified. van der Waals radii were subtracted from the interatomic distances, yielding an estimate of the "free space" at both faces of each radical carbon in each snapshot. These free space estimates were averaged across the last 7.4 ns of the trajectories.

RESULTS

Spin Localization in the Substrate-Derived Radical. Previous studies have demonstrated a connection between calculated spin distribution and product distribution and indicate that oxygen preferentially adds to delocalized radicals at the site bearing the highest spin density (*7*, *35*). We initially focused on the idea that enzyme-enforced spin localization in the substrate-derived AA-13-yl radical might explain the regio- and stereoselectivity of the COX-catalyzed oxygenation of AA. Since maximum delocalization of the unpaired electron spin requires optimal (parallel) overlap (alignment) of the $2p_z$ orbitals on the five radical carbon atoms, distortion of the pentadienyl radical from planarity can alter the spin distribution and thus bias the site to which molecular oxygen will add. If COX bound the AA-13-yl radical in a conformation that forced the C11−C12 bond to rotate away from 0°, this would disrupt the orbital overlap in the C11−C15 pentadienyl radical, resulting in spin localization at the C11 position (Figure 1A). Spin density localization at C11 would provide a simple, straightforward explanation for the regio- and stereoselectivity observed in the COX reaction. Similarly, rotation about the C13−C14 bond would restrict oxygen

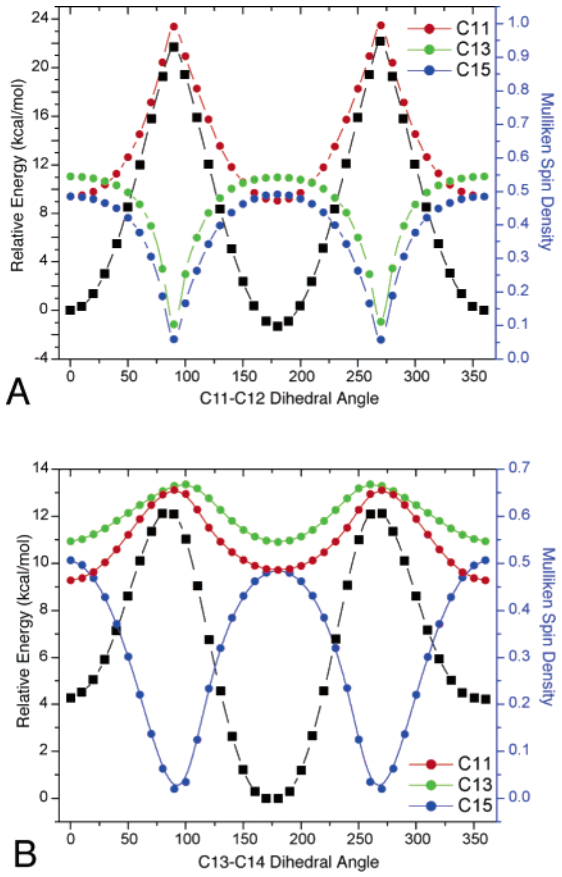

FIGURE 2: (U)B3LYP/6-31G(d) theoretical spin distribution (red, green, and blue circles) along potential energy surfaces (black squares) for rotation about (A) the C11−C12 bond and (B) the C13−C14 bond in the 11,15-dimethyl-*Z*,*Z*-pentadienyl radical (as described in Figure 1). While spin is delocalized among C11, C13, and C15 for torsion angles 0° and 180°, deviation from planarity leads to maximum localization of spin at C11 at 90° and 270° (A) or formation of an allyl radical across C11−C13 (B).

addition to two carbon atoms, C11 and C13, via formation of an allyl radical (Figure 1B).

We utilized density functional theory (DFT) to calculate torsion angle energy profiles for rotation about the C11−C12 and C13−C14 bonds of the AA-13-yl radical, using a pentadienyl radical model system, 2*Z*,5*Z*-heptadienyl radical, for computational efficiency. We used this torsion angle energy profile to correlate the torsion angle distortion energy (i.e., the energetic penalty) with the extent of spin density localization in the pentadienyl radical, and the results are shown in Figure 2. To achieve a significant spin density distribution bias (e.g., 50% greater spin density at C11 compared to C13 or C15), a 55° rotation is required about the C11−C12 bond, with a 10 kcal/mol energy barrier (Figure 2A). Rotation at the C11−C12 bond causes pyramidalization at C11, due to the steric interaction between atoms C10 and C13. The extent of pyramidalization was calculated as the average of three improper torsion angles describing the deviation of the C11 radical center from the plane defined by atoms C10, C12, and H11. At a C11−C12 torsion angle of 55°, pyramidalization at C11 is approximately 16°. A comparable rotation at the C13−C14 bond would generate an allylic radical with approximately 50% greater spin density at the allylic carbons C11 and C13 relative to C15 but would require only 6 kcal/mol since much of the radical stabilization enthalpy is retained upon conversion from a pentadienyl radical to an allylic radical (Figure 2B). However, there is no pyramidalization, and hence no stereochemical preference, in the allylic radical, and spin density is distributed between two carbon atoms as opposed to being localized at one carbon.

With the calculated gas phase results for spin density localization as a function of torsion energy barrier, we next performed MD simulations for the enzyme/AA-13-yl radical complex to determine whether the enzyme is capable of imposing a sufficiently strained ligand conformation in the active site to yield meaningful spin density localization in the radical. We used both equilibrium MD simulations and potential of mean force (PMF) calculations to sample radical conformations in the COX-1 and COX-2 active sites and for the radical free in solution. For the enzyme complex simulations, AA-13-yl intermediates were included in the cyclooxygenase active sites of both monomers of the COX homodimers. To track potential differences in behavior between the individual monomers, we refer to them as monomers A and B in this work (COX-1A, COX-1B, COX-2A ,and COX-2B) and include data for all four individual monomers where appropriate. In the PMF calculations, we used a harmonic restraint to force the C11−C12 and C13−C14 bond rotations to sample a 90° range during the course of MD simulations for both the enzyme complexes and the radical free in solution.

The conformational analysis results for all four AA-13-yl radical torsions, C11−C12, C12−C13, C13−C14, and C14−C15, as well as the two flanking torsions, C10−C11 and C15−C16, are shown in Figure 3. Unlike the conformational dynamics of AA (see accompanying paper), the AA-13-yl radical exhibited very little difference in behavior between COX-1 and COX-2 complexes for the subset of torsion angles monitored here, indicating a decrease in conformational freedom upon conversion to the pentadienyl radical intermediate. While the C10−C11 torsion of the AA-13-yl radical in our simulations is consistent with the COX-1/AA X-ray crystal structure (*17*) (∼240° and 202°, respectively), it differs significantly from the conformation of COX-bound AA-derived pentadienyl radicals proposed by Tsai and coworkers based on EPR data (C10−C11 torsion of ∼0°) (*36*). The latter conformation would require the C10−C11 torsion to overcome a ∼3.8 kcal/mol energy barrier, according to our calculations (see accompanying paper), and is not sampled in our current simulations. Our results for the C15−C16 torsion (∼240°) are in closer agreement with the EPR-based structural prediction of ∼280° (*36*). Both of these values deviate from the COX-1/AA crystallographic value of 131°. Across the radical plane, itself, there was remarkably little difference in conformational behavior when AA-13-yl was free in solution or bound to either enzyme. The averages and standard deviations, as well as maximum and minimum deviations, were all comparable (Figure 3). This suggests that the enzyme active site does not distort the planarity of the radical to a greater degree than the natural fluctuations observed in solution.

The results of the PMF calculations reinforce this conclusion. For the C11−C12 torsion (Figure 4A), there is no difference in the energy barrier to rotation when the AA-13-yl radical is free in solution or bound to COX-1. If COX-1 were able to impose a deviation from planarity in this torsion

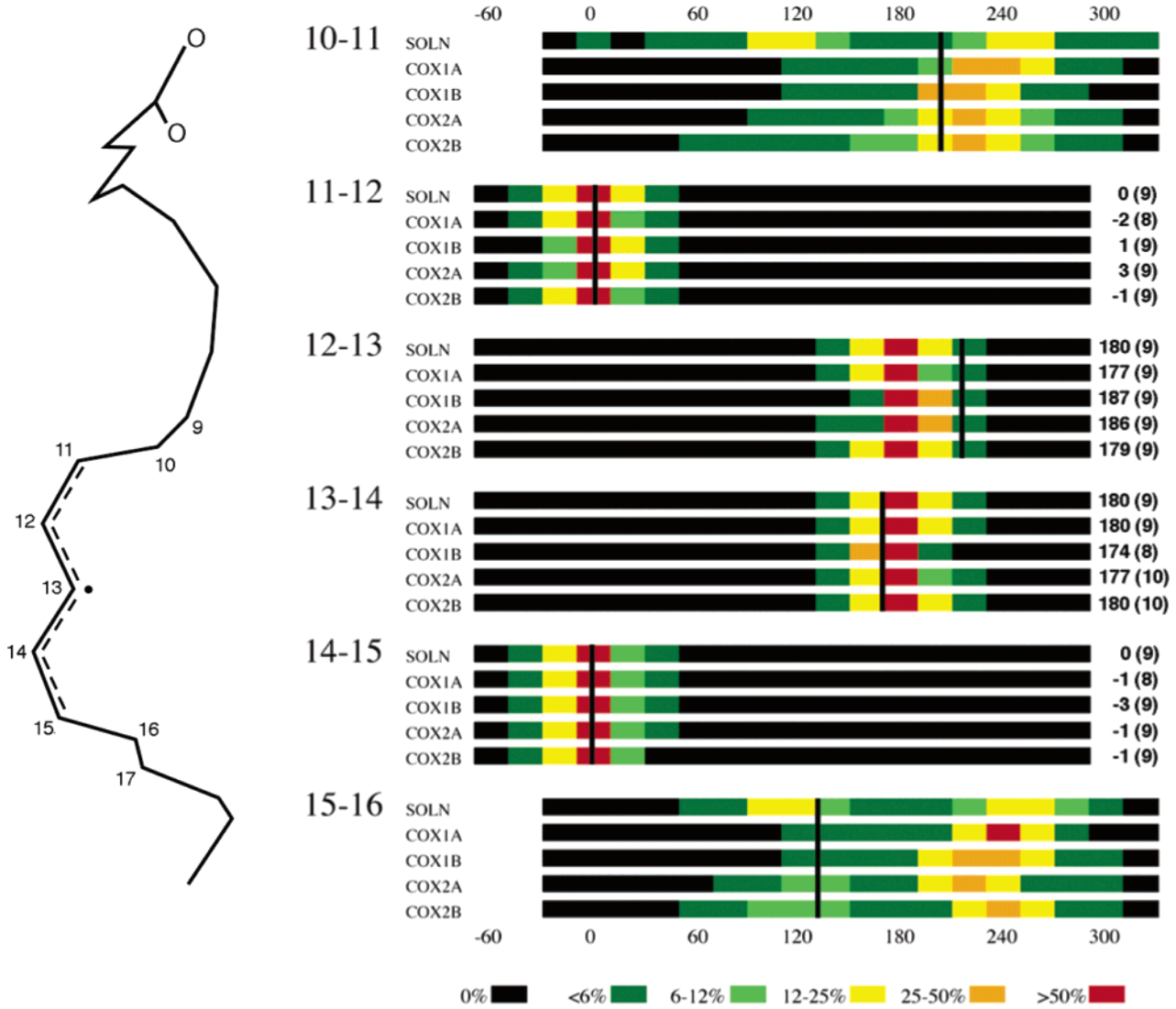

FIGURE 3: Color-coded histograms showing torsion angle sampling for the AA-13-yl radical intermediate simulated free in solution (SOLN) as well as bound to monomers A and B of homodimers COX-1 and COX-2. Colors indicate percentage of the trajectory spent in each torsion angle range. Averages with standard deviations are shown on the right for the four planar pentadienyl radical torsions. The numbers on the left indicate the torsion described, e.g., 10−11 refers to the C9−C10−C11−C12 torsion angle. Vertical black lines indicate the torsion angle value observed in the COX-1/AA complex crystal structure (*17*). The structure of AA-13-yl is shown on the left for reference.

angle, the energy barrier would be expected to be lower in the enzyme-bound profile. The C13−C14 torsion (Figure 4B) is even more dramatic. The energy barrier to rotation in the 180° → 90° direction is ~2 kcal/mol higher in the enzyme-bound PMF profile, suggesting that the enzyme actually reinforces planarity in the pentadienyl moiety, rather than facilitating a rotation to create an allyl radical. Taken together, these results suggest that the COX active site does not control the first oxygen addition by straining the C11−C15 pentadienyl radical to localize spin density on C11 or create an allyl radical across C11−C13.

Oxygen Channeling. Another possible mechanism of control in the COX enzymes would involve the trafficking of oxygen into the cyclooxygenase active site through a specific channel. Although crystal structures of the COX-1 and COX-2 isoforms have been available in the literature for more than 10 years, no oxygen delivery channel has been identified as yet. The available data have inspired the hypothesis that oxygen enters the cyclooxygenase active site through the same channel as does the substrate. We observed three channels connecting the exterior surface of the protein to the cyclooxygenase active site, in addition to the principal substrate access channel (Figure 5). Two of these are smaller channels extending from the upper, distal end of the cyclooxygenase active site to the dimer interface and are thus labeled D1 and D2 in Figure 5. D1 has previously been suggested to act as a release valve for water upon substrate binding (*16*). The third, S1, is a channel extending from the side of the active site opposite that which leads to the dimer interface. This region has been called the side pocket and is known to be larger in COX-2, due to three mutations relative to COX-1 (I523V, R513H, and I434V). We found that this side pocket leads to a channel that opens out into solution in both isoforms. We used the channel_finder utility developed in our previous work to monitor channel opening fluctuations over the course of the final 7.4 ns of each trajectory. This protocol determines the largest spherical particle that can transit the entire channel in each trajectory configuration and reveals a dynamic picture of channel opening/closing events over time. If molecular oxygen is considered to be an ellipsoid molecule, with radii of approximately 1.6 and 2.2 Å along its two principal axes,

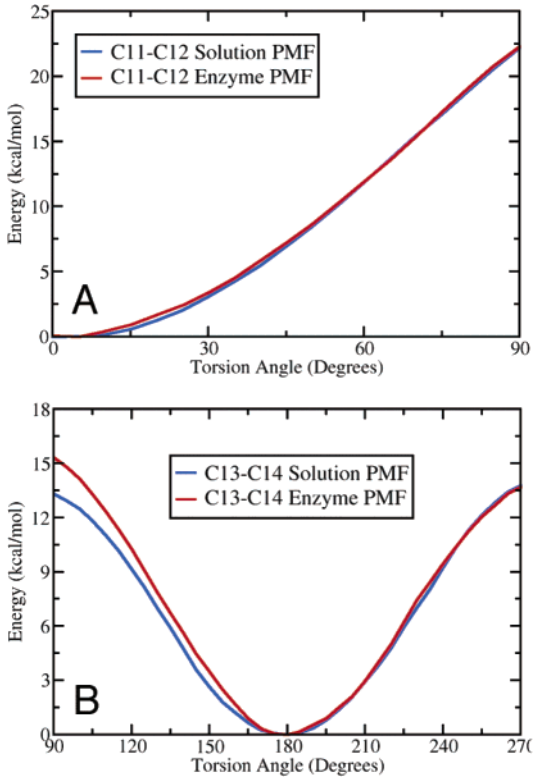

FIGURE 4: Results of potential of mean force (PMF) calculations. Comparison of the energy barriers to rotation about (A) the C11−C12 bond (as in Figures 1A and 2A) and (B) the C13−C14 bond (as in Figures 1B and 2B) of the AA-13-yl radical when bound to COX-1 vs free in solution.

channel openings greater than 1.6 Å in radius are considered to be sufficient for O_2 passage.

Histograms of the channel_finder measurements are shown in Figure 6. The first dimer interface channel, D1, exhibited remarkably consistent behavior for both monomers of both COX-1 and COX-2, demonstrating the least variability of all of the channels measured. The second dimer interface channel, D2, was the only channel to exhibit bimodal distributions of channel widths. The broader of the two observed channel widths is consistent with the X-ray crystal structures of the COX-1/AA and COX-2/AA complexes (*17*, *20*). In our simulations, the narrowing of this channel results from the position of the loop containing Ser-126 and Pro-127. Movement of this loop to constrict the D2 channel is accompanied by minimal perturbation of the surrounding helices, indicating a reasonable amount of flexibility in this region. Both COX-1 monomer A and COX-2 monomer B predominantly displayed the wider configuration, with minor sampling of the narrow one, while COX-1 monomer B and COX-2 monomer A maintained the wider width exclusively. This suggests that narrowing of this channel is not isoform-specific behavior. While both D1 and D2 exhibited a few opening events sufficiently wide for O_2 or H_2O to pass, they are unlikely O_2 channels, as access to the pentadienyl radical is blocked by the tight fit of the distal end of the AA-13-yl chain in the active site.

The side channel, S1, was the only channel to demonstrate isoform-specific differences in the present analysis, indicating that the larger side pocket in COX-2 terminates in a slightly larger channel in/out of the enzyme. In COX-2, S1 opens wider than 1.6 Å in both monomers throughout the trajectory

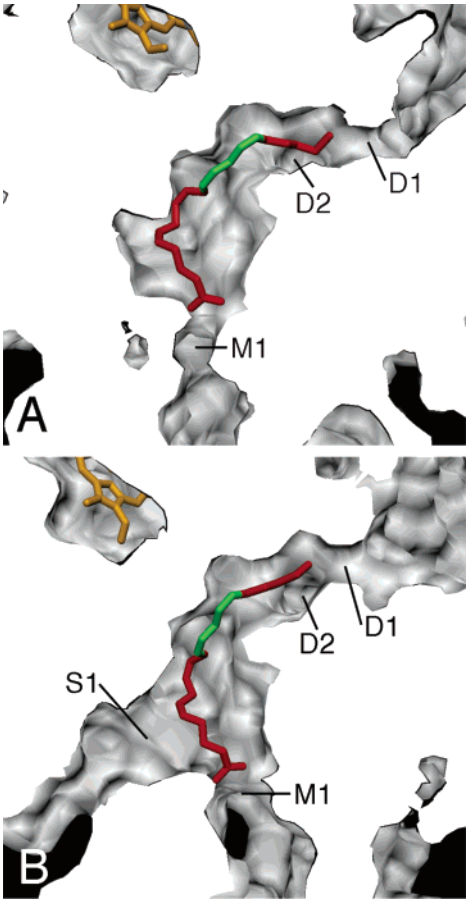

FIGURE 5: Solid surface side views of the cyclooxygenase active site for average structures of COX-1 (A) and COX-2 (B) calculated from MD trajectories. In both panels, arachidonate is shown in red with C11−C15 highlighted in green and heme cofactors in orange. Each structure has been sliced with a vertical clipping plane (cut surface is white) to show the interior cavity surface (gray) and several channels to the exterior of the protein. Main channel M1 is the putative substrate access channel. Channel D2 travels into the plane of the figure, orthogonal to channel D1. Both D1 and D2 lead into the dimer interface. Side channel S1 was closed to the 1.0 Å probe sphere in the COX-1 average structure. This figure and figure 7 were created with DINO (*32*) using surfaces generated with MSMS (*31*).

(COX-2A, 41 times or 0.6%; COX-2B, 1060 times or 14%), suggesting possible function as an O_2 access route. However, this channel remained narrow in COX-1, with no spontaneous opening events larger than 1.4 Å, suggesting that O_2 transport is unlikely. Though COX-1 and COX-2 exhibit conserved differences in their active sites, many of which are in the S1 region and have been exploited in selective drug design, they are believed to share a common mechanism for the conversion of AA to PGH_2. It is therefore unlikely that S1 would serve as an oxygen access route in COX-2 but not COX-1.

The substrate access channel or "main" channel, M1, exhibited openings wide enough for O_2 to pass in both COX-1 and COX-2 (COX-1B, 188 times or 2.5%; COX-2B, 36 times or 0.5%). Interestingly, both isoforms had one monomer that was closed to a probe the size of O_2 and one monomer that was more open, exhibiting a wider distribution of channel widths. The main channel is the most intuitive option for O_2 access, as it leads directly from the membrane, which would have a higher partial pressure of O_2 than the surrounding aqueous environment, and also provides the most

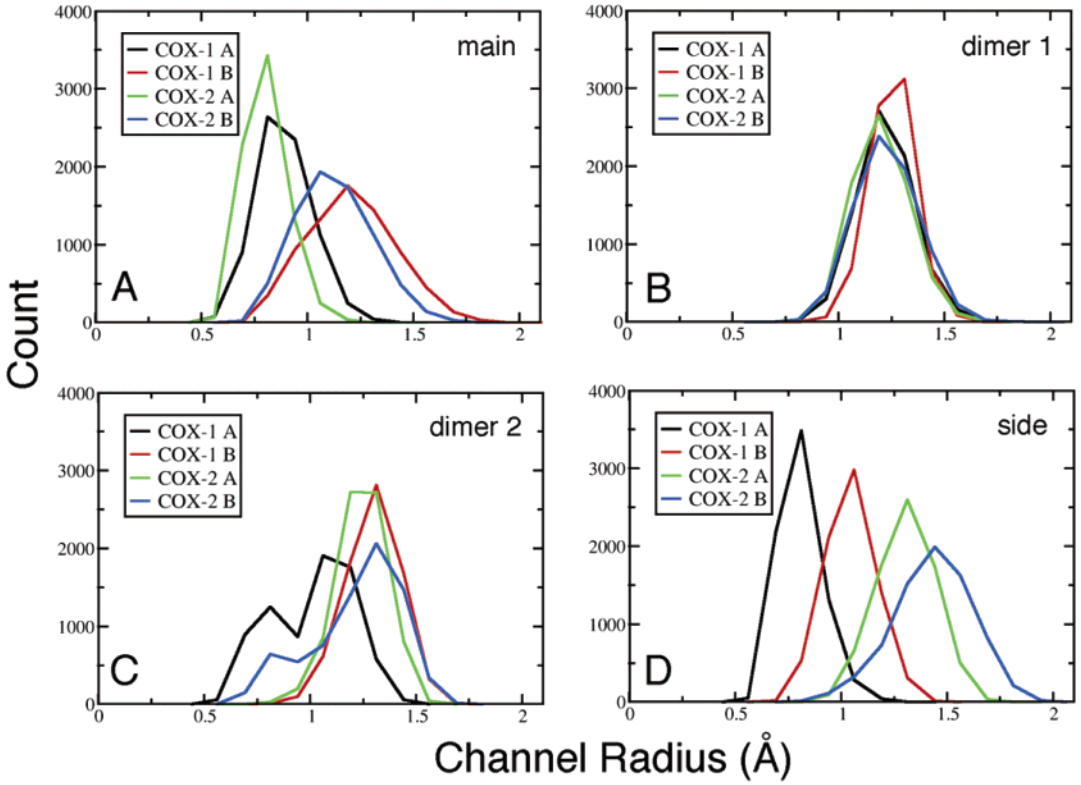

FIGURE 6: Channel radii histograms for the COX-1/AA-13-yl and COX-2/AA-13-yl complex trajectories. Measurements of (A) the main channel (M1) from the lobby region into the active site, (B) the primary dimer interface channel (D1), (C) the second dimer interface channel (D2), and (D) the side channel (S1) that extends from the Ile/Val523 side pocket.

direct access to the *pro-R* face of C11. It is also the most difficult to probe experimentally with mutagenesis, since the main channel is also the proposed access route for substrate.

To supplement the channel measurements, a number of short 500 ps simulations were conducted with an explicit O_2 molecule in the cyclooxygenase active site of each monomer in order to evaluate O_2 mobility within the enzyme and detect any exit/reentry events through the proposed channels. The O_2 molecule was initially placed near the *pro-R* face of C11, the predominant site of the first oxygen addition to the AA-13-yl radical. The O_2 trajectories observed in these simulations are illustrated in Figure 7. Interestingly, exit events were only observed through the main channel. Oxygen was unable to move around the bound AA-13-yl radical to access other channels, even within the slightly larger active site of COX-2. However, in the fourth simulation of COX-2 monomer B, oxygen was able to access the space above the radical plane, though it was not able to travel all the way to the D1/D2 channels. This represented the only configuration in which O_2 was significantly closer to C15 than C11 (4 vs 7 Å, on average), suggesting that oxygen may be able to enter the cyclooxygenase active site through the main channel and access the *pro-R* face of C15 to give the minor, monohydroxy acid product 15*R*-HETE.

The wider M1 channels of monomers B of COX-1 and COX-2 exhibited at least one if not multiple exit events in every simulation, while only a single exit event was observed through the smaller main channel of COX-1 monomer A. COX-2 monomer A displayed the most tightly closed M1 channel during these simulations, and no oxygen exit/reentry events occurred. These results may indicate that main channel width is a better predictor of oxygen access and mobility than active site volume, supporting a common mechanism for these two isoforms, despite the well-established differences in their active sites.

Steric Shielding. The most widely held theory suggests that the regio- and stereoselectivity of the first oxygenation is a result of steric blockage (*17*, *20*). This concept, structurally related to oxygen channeling, suggests that the fatty acid substrate is bound to the enzyme in such a way that only one of the reactive carbon centers of the pentadienyl radical is accessible to molecular oxygen. Indeed, in the X-ray crystal structure of AA bound to COX-1, C11 is positioned above a small pocket of empty space, leaving the *pro-R* face of C11 more exposed than C13 and C15 (*17*). We examined the accessibility of the three reactive carbon atoms over the course of our simulations to determine if this steric shielding profile was maintained over time in our AA-13-yl radical complexes of COX-1 and COX-2. The distance between each AA-13-yl radical carbon and the closest enzyme atom along both faces was estimated for each configuration of the final 7.4 ns of both simulations.

The results of this "free space" analysis, presented in Figure 8, indicated that the greater amount of free space near the *pro-R* face of C11 observed in the COX-1/AA crystal structure was preserved in a dynamic sense in both the COX-1/AA-13-yl and COX-2/AA-13-yl complex simulations. In addition, the entire "top" face of the radical was relatively more shielded than the "bottom" face. Surprisingly, COX-2 monomer B exhibited a minor alternate bound conformation of AA-13-yl (Figure 9). Late in the trajectory, the radical flipped nearly 180° into a pocket where it made good van der Waals contact with Phe-381, Leu-384, Tyr-385, and Trp-387 along the top of the active site. Notably, these four

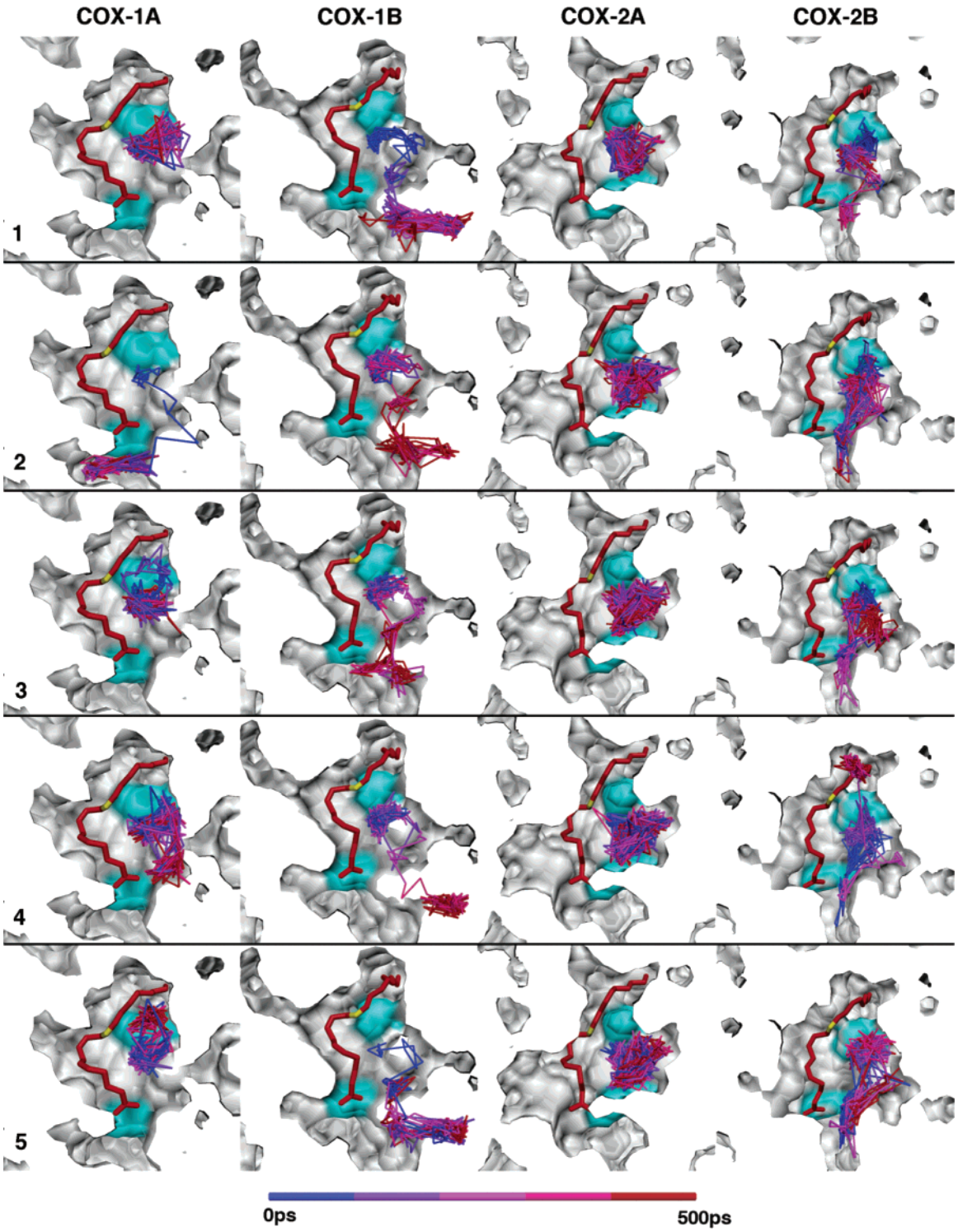

FIGURE 7: Traces of oxygen position from explicit O_2 simulations. Each panel is a sliced solid surface view of the cyclooxygenase active site of COX-1/AA-13-yl (columns 1 and 2) and COX-2/AA-13-yl (columns 3 and 4) complexes in the snapshot used as a starting point for five different trajectories (rows 1−5). The AA-13-yl radical is shown in red, with C11 highlighted in yellow and the surfaces of active site residues Arg-120 (bottom) and Ser-530 (top) highlighted in cyan. The position of O_2 in the active site over time is traced by a line that changes color from blue to red from 0 to 500 ps. While the surface views were sliced with a vertical clipping plane (cut surface is white) to show the interior space, no clipping planes were used on the oxygen traces in order to show them in their entirety. In panels where it appears the trace has traveled outside the channel, it is actually in a part of the channel that lies in front of the clipping plane.

residues were found to contact the endoperoxide ring in a crystal structure of PGG/H_2 bound to murine COX-2 (*20*), indicating that our flipped conformation may place the pentadienyl radical itself in the space needed for the cyclization steps in the conversion to PGG_2. This is supported by experimental evidence that mutation of Leu-384 (to Phe or Trp) disrupts closure of the five-membered carbon ring in prostaglandin synthesis, leading to novel diepoxide products (*37*). Our flipped conformation did not reverse the exposure of the top face of the radical relative to the bottom face. However, it did reverse the relative shielding of the *pro-R* face of C11 vs the *pro-S* face of C15, with C15 now

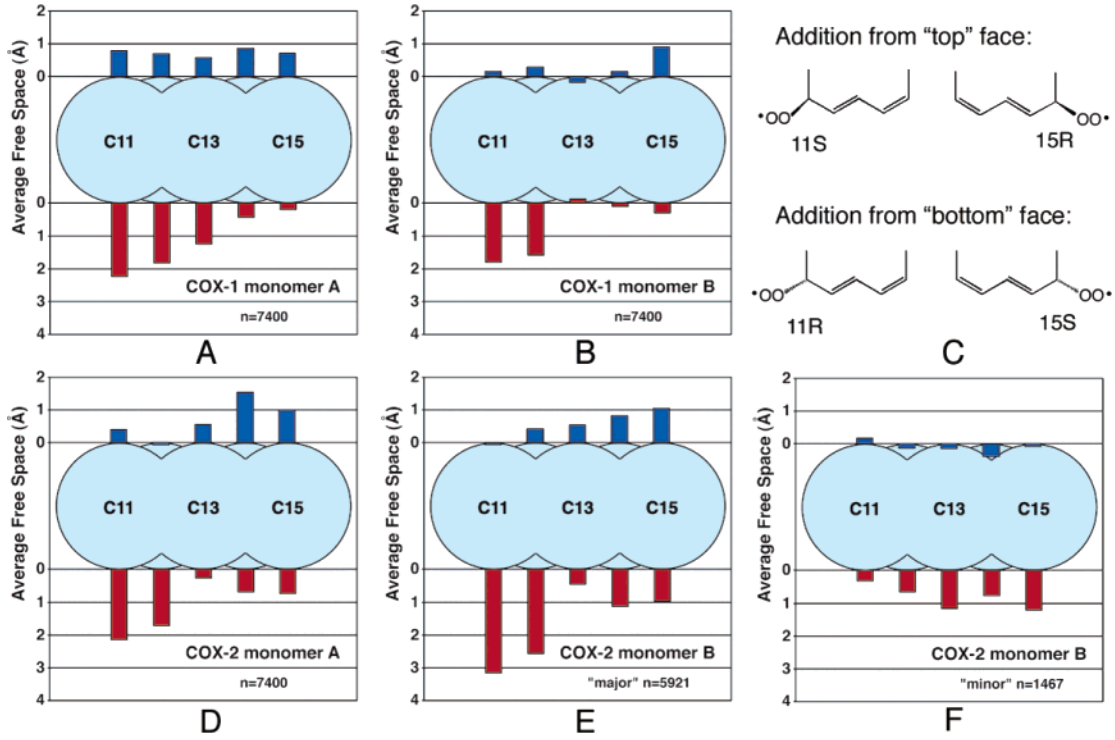

FIGURE 8: Average free space estimates. The amount of empty space along the "top" and "bottom" of the pentadienyl radical carbons (C11−C15) in the COX-1/AA-13-yl and COX-2/AA-13-yl complex trajectories is indicated by the height of the bars. The top face (blue bars) is defined as the face exposed to Tyr-385 (*pro-S* face of C11 and C13, *pro-R* of C15); the bottom face (red bars) is defined as the face exposed to Ser-530 (*pro-R* face of C11 and C13, *pro-S* of C15). The carbon atoms are represented by cyan spheres. COX-2 monomer B exhibited two distinct AA-13-yl conformations, so two panels are shown, representing the major (E) and minor (F) bound conformations.

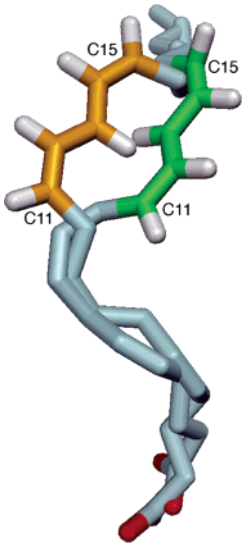

FIGURE 9: Alternate AA-13-yl radical conformation. The major and minor bound conformers of AA-13-yl in the COX-2 monomer B simulation are shown with carbons in cyan, hydrogens in gray, and oxygens in red, with the pentadienyl radical carbons (C11−C15) of the major conformer highlighted in green and the minor conformer in orange.

exhibiting a slightly greater amount of free space. It has been suggested that alternate bound conformations of AA could lead to the minor products, 11*R*-HETE and 15*R*/*S*-HETE (*38*). The alternate AA-13-yl position we observe here may provide a plausible mechanistic explanation for these minor products, since this alternate bound conformation would simultaneously encourage addition to the *pro-R* face of C11 or *pro-S* face of C15, while discouraging cyclization by occupying the region of the active site that contacts the endoperoxide ring of PGG_2.

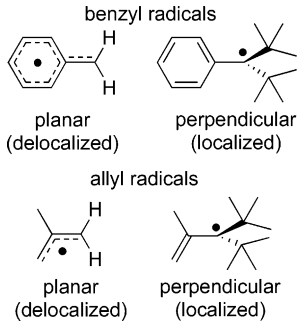

FIGURE 10: Structures of benzyl and allyl radicals wherein the unpaired electron spin is either delocalized over multiple carbon atoms or localized to a single carbon atom (*39*, *40*).

DISCUSSION

It is known that changes in the geometry of planar radicals can alter spin density distribution. For example, the benzyl radical preferentially adopts a conformation in which the $2p_z$ orbitals of all seven carbon atoms combine to form molecular orbitals that allow maximum delocalization of the unpaired electron spin. However, in the 1,1-di-*tert*-butylbenzyl radical, steric interactions between the bulky *tert*-butyl groups and the ortho aromatic hydrogens lead to a conformation in which the $2p_z$ orbital of the benzylic carbon atom is orthogonal to the phenyl ring π-system, localizing unpaired electron spin on the benzylic carbon atom (Figure 10A) (*39*). The 1,1-di-*tert*-butyl-2-methylallyl radical exhibits a similar conformational preference, resulting in a localized carbon-centered

Scheme 4: Competing Pathways in the Formation of Oxidation Products from AA-13-yl in the PGHSs

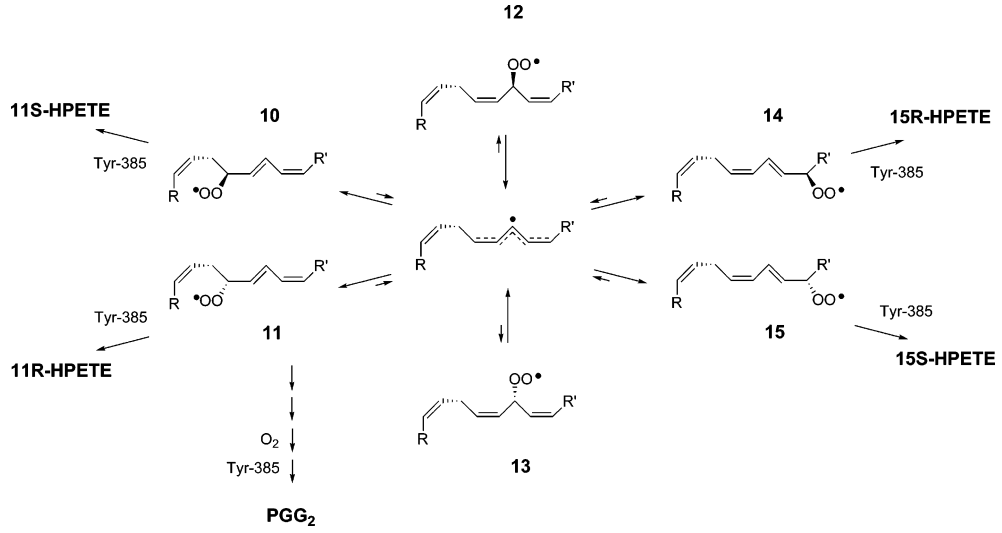

radical instead of a delocalized allyl radical (Figure 10B) (*40*).

Spin localization through radical torsion would provide a simple and elegant explanation for the regio- and stereoselectivity of oxygenation of AA in the normal turnover of the COX enzymes. Tsai and co-workers have reported EPR signals consistent with a twisted allyl radical intermediate in single-turnover experiments with COX-1 and aspirin-acetylated COX-2 but not unmodified COX-2 (*41*). Interestingly, these signals were found to be isotope-sensitive; the same experiments with AA-d_8 lead to pentadienyl radicals. EPR spectral features consistent with an allyl radical intermediate have also been observed in lipoxygenase (LOX) catalysis (*42*). However, we have found no evidence of preference for a spin-biased conformation in MD simulations of COX-1 and COX-2 complexes with the AA-13-yl radical. Instead, the results suggest a maximally delocalized pentadienyl radical intermediate, whose deviations from planarity fall within those accounted for by thermal fluctuations and do not differ from those exhibited by the AA-13-yl radical free in solution. We also did not observe isoform-specific differences in the behavior of the pentadienyl radical that could account for the difference in EPR signal reported for unlabeled AA bound to COX-1 vs COX-2 (*41*). Simulation of the AA-13-yl radical bound to acetylated COX-2 could potentially yield more insight into the EPR signal that has been interpreted as a twisted allyl radical.

The delivery of molecular oxygen to the cyclooxygenase active site through a specific channel represents another potential control mechanism. Such channels have been described for a number of enzymes, including soybean LOX (*43*, *44*). Solvent-accessible surface calculations on the COX enzymes reveal four primary channels leading from the surface of the protein to the cyclooxygenase active site. Inclusion of molecular oxygen in the simulations revealed that O_2 could only escape the active site of the protein through the putative substrate access channel (M1) and that the most likely site of attack would be the *pro-R* face of C11, although O_2 was able to access the *pro-R* face of C15 in 1 out of 20 simulations. The oxygen mobility studies do not support involvement of the other three channels in directing molecular oxygen to the active site. Measurement of the width of these channels across the trajectories supports this conclusion, as M1 was the only channel to display a significant number of opening events large enough for O_2 to transit in both isoforms. The results of the present channel measurements are fully consistent with our earlier results for COX-1 and COX-2 complexes with AA, indicating that the change from bound AA to AA-13-yl radical intermediate does not bring about a dramatic change in channel behavior, at least on a nanosecond time scale.

Alteration of the steric environment through mutation of active site residues has been shown to affect enzymatic control of reactions. In LOX catalysis, reduction in steric bulk around the pentadienyl radical intermediate markedly decreased both the regio- and stereospecificity of oxygenation (*44*). Mutagenesis has been used to characterize the roles of most of the residues lining the cyclooxygenase active site, some of which are capable of altering the ratio of prostaglandins to 11*R*- and 15*R/S*-HETE products (*45*). Schneider et al. have identified two residues, Ser-530 and Val-349, that control the stereochemistry of the second oxygen addition at C15 (*46*), and two, Leu-384 and Gly-526, that can arrest the normal cyclizations to produce novel products when steric bulk is added (*37*). However, no mutant has been reported to alter the stereochemistry of the first oxygen addition at C11; when oxygen adds to C11, it adds to the *pro-R* face exclusively. Our present steric shielding analysis revealed the *pro-R* face of C11 to be the most exposed of the positive spin-bearing positions along the AA-13-yl radical, while the *pro-S* face of C11 was the most shielded, indicating that steric shielding is an important factor in control of the stereochemistry of oxygenation at C11. However, the shielding profiles indicated modest exposure of C13, often comparable to that of C15, so shielding alone does not appear to explain why no 13-HETE products have been observed.

These analyses contribute to an emerging picture in which the enzyme narrows the range of potential products by channeling oxygen to the bottom face of the AA-13-yl radical via the substrate access channel and then sterically shields the undesirable sites of addition. However, the simulations also suggest that these control mechanisms are imperfect. While it is possible that such control lapses could occur at a frequency that accounts for the minor 11- and 15-HPETE

products, there remains one other possibility that has received little attention in the literature. Given the mechanistic studies on linoleate autoxidation (*3*, *5*−*7*), it seems reasonable to propose that oxygen adds freely to the accessible faces of C11, C13, and C15 of the pentadienyl radical, and it is the kinetics of the competing follow-up reactions of the intermediate peroxyl radicals that are responsible for the regio- and stereochemical outcome of the enzymatic reaction (Scheme 4).

Approximate lower bounds for rate constants that dictate the fate of each of the intermediate peroxyl radicals can be estimated from existing solution-phase work. Once formed, the nonconjugated peroxyl radicals **12** and **13**, resulting from oxygenation at C13, can be expected to undergo rapid β-fragmentation back to the AA-13-yl radical and molecular oxygen with a rate constant exceeding 2×10^6 s^{-1} (*7*), whereas the conjugated peroxyl radicals **10**, **11**, **14**, and **15**, resulting from oxygenation at C11 or C15, β-fragment back to the AA-13-yl radical and molecular oxygen with a rate constant of only 430 s^{-1} (*47*). In competition with these "reverse" or "nonproductive" reactions are trapping of the peroxyl radicals with a hydrogen atom from Tyr-385 or, in the case of addition at the C11 position, intramolecular 5-*exo* radical cyclization to form the endoperoxide ring. The 5-*exo* cyclization can be expected to proceed with a rate constant >800 s^{-1} based on solution measurements (*3*, *5*−*7*). The rate constant for the reaction of Tyr-385 with the intermediate peroxyl radicals can be estimated at 10000 M^{-1} s^{-1}, based on the solution rate constant for the reaction of 4-methylphenol with alkylperoxyl radicals (*48*, *49*). While these estimations suggest cyclization to be a factor of $\sim$10 slower than hydrogen atom transfer from Tyr-385, both cyclization and β-fragmentation are unimolecular processes that require little geometric organization to proceed. Despite the proximity of Tyr-385, we expect the geometric constraints of the bimolecular reaction to be more significant to overcome and experience the least acceleration upon going from solution to the enzyme active site.

Since the intermediate C13−OO$^\bullet$ peroxyl radical is expected to undergo a very rapid β-fragmentation reaction to regenerate the pentadienyl radical and O_2, it is reasonable that 13-HPETE may never be observed due to the lack of an active site residue that is sufficiently reactive to peroxyl radicals to trap it. The predominance of prostaglandin products is likely due to the rate acceleration of the 5-*exo* cyclization of the intermediate *R*-C11−OO$^\bullet$ onto the C8/9 double bond over simple reduction to give 11*R*-HPETE. The fact that no 11*S*-HETE is observed suggests that O_2 never contacts the *pro-S* side of C11 and that a combination of simple competition kinetics and oxygen channeling/steric shielding is required to explain the regio- and stereochemical preference of the first oxygenation by the cyclooxygenase active site. We should note that spin localization through radical torsion may be important in the second oxygenation, HETE production in aspirin-acetylated COX-2, or in the oxygenation of linoleic and arachidonic acids by the LOX enzymes. We are currently exploring these ideas further.

The rate-limiting step in the cyclooxygenase reaction is thought to be the stereospecific abstraction of the arachidonate C13 *pro*-S hydrogen atom (*15*). Our current simulations provide some interesting suggestions regarding enzymatic control for this key step but do not allow us to probe mechanistic issues for subsequent steps in the reaction. Additional simulations are in progress to examine some aspects of subsequent steps. We cannot extract any detailed kinetic information for the reaction from these simulations, as this would require far more extensive sampling than we have performed to date and is quite challenging. We do know that, in the solution reaction, hydrogen atom abstraction (i.e., hydrogen atom transfer) is slow compared to oxygen addition and radical cyclization reactions (*5*), and this is presumably the case in cyclooxygenase-catalyzed reactions as well.

ACKNOWLEDGMENT

We thank Dr. Larry Marnett for helpful discussion and Dr. Jarrod Smith for help in writing the channel_finder utility.

SUPPORTING INFORMATION AVAILABLE

Potential function parameters for the substrate-derived pentadienyl radical in the form of frcmod and prep files and RMSD vs time plots for COX-1/AA-13-yl and COX-2/AA-13-yl trajectories. This material is available free of charge via the Internet at http://pubs.acs.org.

REFERENCES

1. Rouzer, C. A., and Marnett, L. J. (2003) Mechanism of free radical oxygenation of polyunsaturated fatty acids by cyclooxygenases, *Chem. Rev. 103*, 2239−2304.
2. Brash, A. R. (1999) Lipoxygenases: Occurrence, functions, catalysis, and acquisition of substrate, *J. Biol. Chem. 274*, 23679−23682.
3. Porter, N. A. (1986) Mechanisms for the autoxidation of polyunsaturated lipids, *Acc. Chem. Res. 19*, 262−268.
4. Funk, C. D. (2001) Prostaglandins and leukotrienes: Advances in eicosanoid biology, *Science 294*, 1871−1875.
5. Porter, N. A., Caldwell, S. E., and Mills, K. A. (1995) Mechanisms of free radical oxidation of unsaturated lipids, *Lipids 30*, 277−290.
6. Brash, A. (2000) Autoxidation of methyl linoleate: Identification of the bis-allylic 11-hydroperoxide, *Lipids 35*, 947−952.
7. Tallman, K. A., Pratt, D. A., and Porter, N. A. (2001) Kinetic products of linoleate peroxidation: rapid β-fragmentation of nonconjugated peroxyls, *J. Am. Chem. Soc. 123*, 11827−11828.
8. Bascetta, E., Gunstone, F. D., and Walton, J. C. (1983) An electron spin resonance study of fatty acids and esters. Part 1. Hydrogen abstraction from olefininc and acetylenic long-chain esters, *J. Chem. Soc., Perkin Trans. 2*, 603−613.
9. Porter, N. A., Weber, B. A., Weenen, H., and Khan, J. A. (1980) Autoxidation of polyunsaturated lipids. Factors controlling the stereochemistry of product hydroperoxides, *J. Am. Chem. Soc. 102*, 5597−5601.
10. Yin, H., Havrilla, C. M., Morrow, J. D., and Porter, N. A. (2002) Formation of isoprostane bicyclic endoperoxides from the autoxidation of cholesteryl arachidonate, *J. Am. Chem. Soc. 124*, 7745−7754.
11. Havrilla, C. M., Hachey, D. L., and Porter, N. A. (2000) Coordination (Ag^+) ion spray-mass spectrometry of peroxidation products of cholesterol linoleate and cholesterol arachidonate: High-performance liquid chromatography−mass spectrometry analysis of peroxide products from polyunsaturated lipid autoxidation, *J. Am. Chem. Soc. 122*, 8042−8055.
12. Hecker, M., Ullrich, V., Fischer, C., and Meese, C. O. (1987) Identification of novel arachidonic acid metabolites formed by prostaglandin H synthase, *Eur. J. Biochem. 169*, 113−123.
13. Xiao, G., Tsai, A. L., Palmer, G., Boyar, W. C., Marshall, P. J., and Kulmacz, R. J. (1997) Analysis of hydroperoxide-induced tyrosyl radicals and lipoxygenase activity in aspirin-treated human prostaglandin H synthase-2, *Biochemistry 36*, 1836−1845.
14. van der Donk, W. A., Tsai, A. L., and Kulmacz, R. J. (2002) The cyclooxygenase reaction mechanism, *Biochemistry 41*, 15451−15458.

15. Hamberg, M., and Samuelsson, B. J. (1967) On the mechanism of the biosynthesis of prostaglandin E_1 and $F_1\alpha$, *J. Biol. Chem. 242*, 5336−5343.
16. Picot, D. (1998) The three-dimensional structure of cyclooxygenases, *Lung Biol. Health Dis. 114* (Eicosanoids, Aspirin and Asthma), 161−186.
17. Malkowski, M. G., Ginell, S. L., Smith, W. L., and Garavito, R. M. (2000) The productive conformation of arachidonic acid bound to prostaglandin synthase, *Science 289*, 1933−1937.
18. Peng, S., Okeley, N. M., Tsai, A. L., Wu, G., Kulmacz, R. J., and van der Donk, W. A. (2001) Structural characterization of a pentadienyl radical intermediate formed during catalysis by prostaglandin H synthase-2, *J. Am. Chem. Soc. 123*, 3609−3610.
19. Peng, S., Okeley, N. M., Tsai, A. L., Wu, G., Kulmacz, R. J., and van der Donk, W. A. (2002) Synthesis of isotopically labeled arachidonic acids to probe reaction mechanism of prostaglandin H synthase, *J. Am. Chem. Soc. 124*, 10785−10796.
20. Kiefer, J. R., Pawlitz, J. L., Moreland, K. T., Stegeman, R. A., Hood, W. F., Gierse, J. K., Stevens, A. M., Goodwin, D. C., Rowlinson, S. W., Marnett, L. J., Stallings, W. C., and Kurumbail, R. G. (2000) Structural insights into the stereochemistry of the cyclooxygenase reaction, *Nature 405*, 97−101.
21. Wang, J., Cieplak, P., and Kollman, P. A. (2000) How well does a restrained electrostatic potential (RESP) model perform in calculating conformational energies of organic and biological molecules?, *J. Comput. Chem. 21*, 1049−1074.
22. Frisch, M. J., Trucks, G. W., Schlegel, H. B., Scuseria, G. E., Robb, M. A., Cheeseman, J. R., Zakrzewski, V. G., Montgomery, J. A., Jr., Stratmann, R. E., Burant, J. C., Dapprich, S., Millam, J. M., Daniels, A. D., Kudin, K. N., Strain, M. C., Farkas, O., Tomasi, J., Barone, V., Cossi, M., Cammi, R., Mennucci, B., Pomelli, C., Adamo, C., Clifford, S., Ochterski, J., Petersson, G. A., Ayala, P. Y., Cui, Q., Morokuma, K., Malic, D. K., Rabuck, A. D., Raghavachari, K., Foresman, J. B., Cioslowski, J., Ortiz, J. V., Baboul, A. G., Stefanov, B. B., Liu, G., Liashenko, A., Piskorz, P., Komaromi, I., Gomperts, R., Martin, R. L., Fox, D. J., Keith, T., Al-Laham, M. A., Peng, C. Y., Nanayakkara, A., Challacombe, M., Gill, P. M. W., Johnson, B., Chen, W., Wong, M. W., Andres, J. L., Gonzalez, C., Head-Gordon, M., Replogle, E. S., and Pople, J. A. (1998) Gaussian, Inc., Pittsburgh, PA.
23. Becke, A. D. (1993) Density-functional thermochemistry. III. The role of exact exchange, *J. Chem. Phys. 98*, 5648−5652.
24. Cornell, W. D., Cieplak, P., Bayly, C. I., Gould, I. R., Merz, K. M., Jr., Ferguson, D. M., Spellmeyer, D. C., Fox, T., Caldwell, J. W., and Kollman, P. A. (1995) A second generation force field for the simulation of proteins, nucleic acids, and organic molecules, *J. Am. Chem. Soc. 117*, 5179−5197.
25. Case, D. A., Pearlman, D. A., Caldwell, J. W., Cheatham, T. E., III, Wang, J., Ross, W. S., Simmerling, C. L., Darden, T. A., Merz, K. M., Stanton, R. V., Cheng, A. L., Vincent, J. J., Crowley, M., Tsui, V., Gohlke, H., Radmer, R. J., Duan, Y., Pitera, J., Massova, I., Seibel, G. L., Singh, U. C., Weiner, P. K., and Kollman, P. A. (2002) AMBER 7, University of California, San Francisco.
26. Berendsen, H. J. C., Grigera, J. R., and Straatsma, T. P. (1987) The missing term in effective pair potentials, *J. Phys. Chem. 91*, 6269−6271.
27. Ryckaert, J. P., Ciccotti, G., and Berendsen, H. J. C. (1977) Numerical-integration of Cartesian equations of motion of a system with constraints—molecular-dynamics of N-alkanes, *J. Comput. Phys. 23*, 327−341.
28. Berendsen, H. J. C., Postma, J. P. M., van Gunsteren, W. F., DiNola, A., and Haak, J. R. (1984) Molecular dynamics with coupling to an external bath, *J. Chem. Phys. 81*, 3684−3690.
29. Darden, T., York, D., and Pedersen, L. (1993) Patical mesh Ewald: An N-log(N) method for Ewald sums in large systems, *J. Chem. Phys. 98*, 10089−10092.
30. Callahan, T. J., Swanson, E., and Lybrand, T. P. (1996) MD display: An interactive graphics program for visualization of molecular dynamics trajectories, *J. Mol. Graphics 14*, 39−41.
31. Kumar, S., Rosenberg, J. M., Bouzida, D., Swendsen, R. H., and Kollman, P. A. (1995) Multidimensional free-energy calculations using the weighted histogram analysis method, *J. Comput. Chem. 16*, 1339−1350.
32. Grossfield, A. (2003) WHAM Version 1.2, Washington University, St. Louis, MO.
33. Sanner, M. F., Spehner, J.-C., and Olson, A. J. (1996) Reduced surface: An efficient way to compute molecular surfaces, *Biopolymers 38*, 305−320.
34. Philippsen, A. (2003) DINO: Visualizing Structural Biology (http://www.dino3d.org).
35. Pratt, D. A., Mills, J. H., and Porter, N. A. (2003) Theoretical calculations of carbon−oxygen bond dissociation enthalpies of peroxyl radicals formed in the autoxidation of lipids, *J. Am. Chem. Soc. 125*, 5801−5810.
36. Tsai, A., Palmer, G., Xiao, G., Swinney, D. C., and Kulmacz, R. J. (1998) Structural characterization of arachadonyl radicals formed by prostaglandin H synthase-2 and prostaglandin H synthase-1 reconstituted with mangano protoporphyrin IX, *J. Biol. Chem. 273*, 3888−3894.
37. Schneider, C., Boeglin, W. E., and Brash, A. R. (2004) Identification of two cyclooxygenase active site residues, leucine 384 and glycine 526, that control carbon ring cyclization in prostaglandin biosynthesis, *J. Biol. Chem. 279*, 4404−4414.
38. Thuresson, E. D., Lakkides, K. M., and Smith, W. L. (2000) Different catalytically competent arrangements of arachidonic acid within the cyclooxygenase active site of prostaglandin endoperoxide H synthase-1 lead to the formation of different oxygenated products, *J. Biol. Chem. 275*, 8501−8507.
39. Schreiner, K., and Berndt, A. (1974) EPR spectrum of a perpendicular benzyl radical, *Angew. Chem., Int. Ed. 13*, 144−145.
40. Regenstein, H., and Berndt, A. (1974) Homohyperconjugation in a perpendicular allyl radical, *Angew. Chem., Int. Ed. 13*, 145−146.
41. Tsai, A., Palmer, G., Wu, G., Peng, S., Okeley, N. M., van der Donk, W. A., and Kulmacz, R. J. (2002) Structural characterization of arachidonyl radicals formed by aspirin-treated prostaglandin H synthase-2, *J. Biol. Chem. 277*, 38311−38321.
42. Nelson, M. J., Cowling, R. A., and Seitz, S. P. (1994) Structual characterization of alkyl and peroxyl radicals in sollutions of purple lipoxygenase, *Biochemistry 33*, 4966−4973.
43. Minor, W., Steczko, J., Stec, B., Otwinowski, Z., Bolin, J. T., Walter, R., and Axelrod, B. (1996) Crystal structure of soybean lipoxygenase L-1 at 1.4 Å resolution, *Biochemistsry 35*, 10687−10701.
44. Knapp, M. J., Seebeck, F. P., and Klinman, J. P. (2001) Steric control of oxygenation regiochemistry in soybean lipoxygenase-1, *J. Am. Chem. Soc. 123*, 2931−2932.
45. Thuresson, E. D., Lakkides, K. M., Rieke, C. J., Sun, Y., Wingerd, B. A., Micielli, R., Mulichak, A. M., Malkowski, M. G., Garavito, R. M., and Smith, W. L. (2001) Prostaglandin endoperoxide H synthase-1: The functions of cyclooxygenase active site residues in the binding, positioning, and oxygenation of arachidonic acid, *J. Biol. Chem. 276*, 10347−10357.
46. Schneider, C., Boeglin, W. E., Prusakiewicz, J. J., Rowlinson, S. W., Marnett, L. J., Samel, N., and Brash, A. R. (2002) Control of prostaglandin stereochemistry at the 15-carbon by cyclooxygenases-1 and 2, *J. Biol. Chem. 277*, 478−485.
47. Porter, N. A., and Wujek, D. G. (1984) Autoxidation of polyunsaturated fatty acids, an expanded mechaistic study, *J. Am. Chem. Soc. 106*, 2626−2629.
48. Chenier, J. H. B., Furimsky, E., and Howard, J. A. (1974) Arrhenius parameters for reaction of the *tert*-butylperoxy and 2-ethyl-2-propylperoxy radicals with some nonhindered phenols, aromatic amines, and thiophenols, *Can. J. Chem. 52*, 3682−3688.
49. Burton, G. W., Doba, T., Gabe, E. J., Hughes, L., Lee, F. L., Prasad, L., and Ingold, K. U. (1985) Autoxidation of biological molecules. 4. Maximizing the antioxidant activity of phenols, *J. Am. Chem. Soc. 107*, 7053−7065.
50. Furse, K. E., Pratt, D. A., Porter, N. A., and Lybrand, T. P. (2006) Molecular dynamics simulations of arachidonic acid complexes with COX-1 and COX-2: Insights into equilibrium behavior, *Biochemistry 45*, 3189−3205.

BI052338H